AIP Journal of Applied Physics

High-electron-mobility GaN grown on free-standing GaN templates by ammonia-based molecular beam epitaxy

Erin C. H. Kyle, Stephen W. Kaun, Peter G. Burke, Feng Wu, Yuh-Renn Wu, and James S. Speck

Citation: Journal of Applied Physics **115**, 193702 (2014); doi: 10.1063/1.4874735
View online: http://dx.doi.org/10.1063/1.4874735
View Table of Contents: http://scitation.aip.org/content/aip/journal/jap/115/19?ver=pdfcov
Published by the AIP Publishing

Articles you may be interested in

N-type conductivity and properties of carbon-doped InN(0001) films grown by molecular beam epitaxy
J. Appl. Phys. **113**, 033501 (2013); 10.1063/1.4775736

Effect of dislocations on electron mobility in AlGaN/GaN and AlGaN/AlN/GaN heterostructures
Appl. Phys. Lett. **101**, 262102 (2012); 10.1063/1.4773510

Effect of dislocation scattering on the transport properties of InN grown on GaN substrates by molecular beam epitaxy
Appl. Phys. Lett. **89**, 162110 (2006); 10.1063/1.2364456

Mg doping of GaN layers grown by plasma-assisted molecular-beam epitaxy
Appl. Phys. Lett. **76**, 718 (2000); 10.1063/1.125872

On the incorporation of Mg and the role of oxygen, silicon, and hydrogen in GaN prepared by reactive molecular beam epitaxy
J. Appl. Phys. **82**, 219 (1997); 10.1063/1.365801

AIP Journal of Applied Physics

Journal of Applied Physics is pleased to announce **André Anders** as its new Editor-in-Chief

[This article is copyrighted as indicated in the article. Reuse of AIP content is subject to the terms at: http://scitation.aip.org/termsconditions. Downloaded to] IP: 140.112.175.226 On: Tue, 09 Sep 2014 15:31:37

JOURNAL OF APPLIED PHYSICS 115, 193702 (2014)

High-electron-mobility GaN grown on free-standing GaN templates by ammonia-based molecular beam epitaxy

Erin C. H. Kyle,[1,a)] Stephen W. Kaun,[1] Peter G. Burke,[1] Feng Wu,[1] Yuh-Renn Wu,[2] and James S. Speck[1]
[1]*Materials Department, University of California, Santa Barbara, California 93106, USA*
[2]*Institute of Photonics and Optoelectronics, and Department of Electrical Engineering, National Taiwan University, Taipei City 10617, Taiwan*

(Received 31 December 2013; accepted 19 April 2014; published online 20 May 2014)

The dependence of electron mobility on growth conditions and threading dislocation density (TDD) was studied for n^--GaN layers grown by ammonia-based molecular beam epitaxy. Electron mobility was found to strongly depend on TDD, growth temperature, and Si-doping concentration. Temperature-dependent Hall data were fit to established transport and charge-balance equations. Dislocation scattering was analyzed over a wide range of TDDs ($\sim 2\times10^{6}\,\mathrm{cm^{-2}}$ to $\sim 2\times10^{10}\,\mathrm{cm^{-2}}$) on GaN films grown under similar conditions. A correlation between TDD and fitted acceptor states was observed, corresponding to an acceptor state for almost every c lattice translation along each threading dislocation. Optimized GaN growth on free-standing GaN templates with a low TDD ($\sim 2\times10^{6}\,\mathrm{cm^{-2}}$) resulted in electron mobilities of 1265 $\mathrm{cm^2/Vs}$ at 296 K and 3327 $\mathrm{cm^2/Vs}$ at 113 K. © *2014 AIP Publishing LLC*. [http://dx.doi.org/10.1063/1.4874735]

I. INTRODUCTION

III-nitride semiconductors have been applied to high-power, high-frequency transistors,[1–5] as well as green,[6–8] blue,[9] and UV[10,11] laser diodes (LDs) and light-emitting diodes (LEDs). Since their conception, many advances in the performance of these devices have been made through material improvements. These advances include increased optical power output in LDs and LEDs,[12–14] reduced threshold current densities in LDs,[15,16] and higher transconductance and lower leakage in high-electron-mobility transistors (HEMTs).[1–4]

One of the best ways to quantify a material's quality is by measuring the electron mobility. Point defects and threading dislocations will scatter carriers, reducing their mobility. By systemically varying growth conditions, measuring the electron mobility, and modeling the results, we can comprehensively understand how growth impacts material quality—specifically, how different growth conditions change the concentration of defects. Previous studies concerning the bulk electron mobility in GaN used many different growth techniques. The most notable of these studies used hydride vapor phase epitaxy (HVPE), which yielded a room temperature (RT) GaN electron mobility of 1245 $\mathrm{cm^2/Vs}$, the highest value at the time.[17] The highest-reported RT single-layer GaN electron mobilities for other growth techniques are as follows: 1005 $\mathrm{cm^2/Vs}$ by metalorganic chemical vapor deposition (MOCVD),[18] 265 $\mathrm{cm^2/Vs}$ by ammonothermal growth,[19] 1150 $\mathrm{cm^2/Vs}$ by N-rich plasma-assisted molecular beam epitaxy (PAMBE),[20] 1191 $\mathrm{cm^2/Vs}$ by Ga-rich PAMBE,[21] and 560 $\mathrm{cm^2/Vs}$ by ammonia-based molecular beam epitaxy (NH_3-MBE).[22]

NH_3-MBE is a promising growth technique, despite the low electron mobility measured in a previous study.[22] This low electron mobility presents a significant opportunity for an improvement in reported material quality. NH_3-MBE has many attractive features, including a high GaN growth rate and an N-rich growth environment. Vertical leakage in GaN films is minimized when films are grown in the N-rich regime, and growth in the N-rich regime is standard for NH_3-MBE.[23] Growth in the Ga-rich regime is standard for PAMBE, producing structures with more vertical leakage pathways.[24] In comparison with MOCVD, NH_3-MBE offers lower growth temperatures ($\sim$200 °C lower), lower C and H concentrations, and sharper interfaces in GaN films. Unlike MOCVD, NH_3-MBE yields p-GaN without an activation anneal, as a consequence of the low H concentration.[25] III-nitride growth by NH_3-MBE has also produced high-quality electron devices. Among many examples, AlGaN/GaN HEMTs grown by NH_3-MBE have displayed excellent power performance at 4 GHz.[26] p-n junctions grown by NH_3-MBE have shown record low ideality factors.[27] Vertical electron devices, specifically current aperture vertical electron transistors (CAVETs), have also seen benefits from NH_3-MBE regrowth for the p-GaN current blocking layer.[28]

Despite the large body of work quantifying the high quality of NH_3-MBE-grown GaN, surprisingly little work has been done to study the bulk electron mobility of GaN grown by this technique.[22] In this article, we first determine the optimal growth conditions to maximize electron mobility, using GaN-on-sapphire templates with threading dislocation densities (TDDs) of $\sim 5\times10^{8}\,\mathrm{cm^{-2}}$. We then demonstrate the impact of TDD on electron mobility and the unintentional acceptor concentration through two series grown on templates with a wide range of TDDs ($\sim 2\times10^{6}$ to $\sim 2\times10^{10}\,\mathrm{cm^{-2}}$). For both TDD series, the temperature-dependent electron mobilities and carrier concentrations were fit to established scattering equations to analyze dislocation scattering and determine the acceptor-like trap spacing along threading dislocations (TDs). Using optimized NH_3-MBE growth conditions on a free-standing (FS) GaN template with a TDD of

[a)]E-mail: erinkyle@umail.ucsb.edu

 © 2014 AIP Publishing LLC

[This article is copyrighted as indicated in the article. Reuse of AIP content is subject to the terms at: http://scitation.aip.org/termsconditions. Downloaded to] IP: 140.112.175.226 On: Tue, 09 Sep 2014 15:31:37

$\sim 2 \times 10^6\,cm^{-2}$, we demonstrate an electron mobility of 1265 cm^2/Vs at RT.

II. EXPERIMENT

In this study, samples were grown in a Veeco Gen 930 molecular beam epitaxy system. The system has conventional effusion cells for Ga, Si, and Mg. Purified NH_3 was delivered into the growth chamber through an unheated showerhead injector. Growth optimization was performed through systematic variation of the growth temperature and the Si-doping concentration. The samples in the growth optimization series used Lumilog semi-insulating GaN:Fe-on-sapphire templates ($\sim 5 \times 10^8\,cm^{-2}$ TDD). Each template had a p^--i-p^+ isolation structures at the regrowth interface to electrically isolate the active region. Electrical isolation is necessary to ensure negligible conduction through the template or the regrowth interface.

A schematic of the growth structure is shown in Fig. 1. The isolation structure consisted of a 200 nm p^+-GaN ([Mg]: $1 \times 10^{19}\,cm^{-3}$) layer, followed by a 200 nm unintentionally doped (UID) GaN layer and a 100 nm p^--GaN ([Mg]: $1 \times 10^{18}\,cm^{-3}$) layer. Since high Mg doping tends to roughen the growth surface, the UID layer combined with the lightly Mg-doped layer ensured a smooth, resistive surface for the start of active region growth. The active region was an 800-nm-thick, lightly doped n^--GaN layer ([Si]: 3–$5 \times 10^{16}\,cm^{-3}$, unless otherwise specified). The active region was capped with 3 nm of highly doped n^+-GaN ([Si]: $5 \times 10^{18}\,cm^{-3}$) to facilitate the formation of high-quality low-resistance ohmic contacts. Growth of the active region and contact layers proceeded in the step-flow growth mode, which was confirmed through a streaky reflection high-energy electron diffraction (RHEED) pattern. Si-doping and Mg-doping concentrations were determined through secondary ion mass spectroscopy.

When the growth optimization series were completed, two TDD series were grown using the established optimal growth parameters. Previous work has shown that NH_3 flow rates ranging from 200 to 1000 SCCM yield high-quality material.[23,29] The TDD-200 series was grown with an NH_3 flow rate of 200 SCCM, and the TDD-1000 series was grown with an NH_3 flow rate of 1000 SCCM. The growth structure shown in Fig. 1 was used for both TDD series. For the low-TDD films, FS GaN templates were provided by two different vendors. The FS GaN template that had a TDD of $\sim 3 \times 10^7\,cm^{-2}$ was produced by Lumilog. The FS GaN template that had a TDD of $\sim 2 \times 10^6\,cm^{-2}$ was produced by Furukawa Electric. The medium-TDD films were grown on Lumilog semi-insulating GaN:Fe-on-sapphire templates with TDDs of $\sim 5 \times 10^8\,cm^{-2}$. For the high-TDD films, GaN templates were grown on 6H-SiC, as described elsewhere.[30,31] The GaN-on-SiC templates had TDDs of $\sim 5 \times 10^9$ and $\sim 2 \times 10^{10}\,cm^{-2}$.

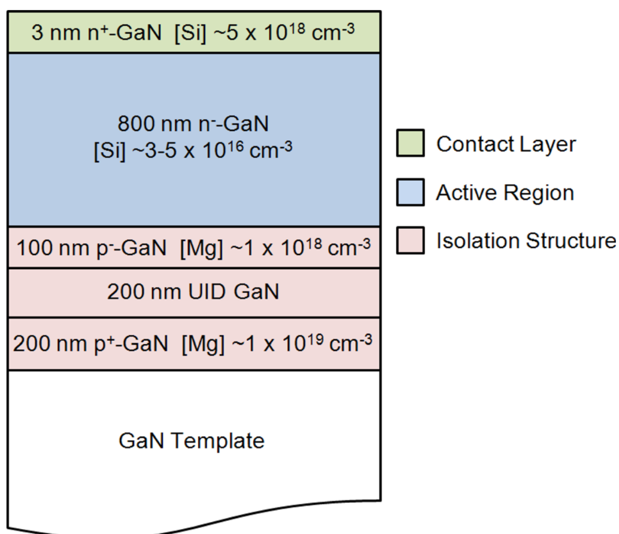

FIG. 1. Schematic of the growth structure. The active region is 800 nm of n^--GaN. The p^--i-p^+ structure (p^--GaN/UID GaN/p^+-GaN) is used to isolate the active region from the regrowth interface. The contact region is created with the 3 nm n^+ layer.

Atomic force microscopy (AFM) was used to characterize the surface morphology. High resolution x-ray diffraction (HRXRD) was used to confirm the TDDs of the films. The rocking curve full widths at half maximum (FWHMs) of HRXRD ω-scans for the GaN $(20\bar{2}1)$ reflection (measured in a skew symmetric geometry) were previously found to correlate to the density of edge-component TDs, which dominate the overall TDD.[32] TDDs were confirmed by a calibration curve linking HRXRD data to TDDs determined by plan-view transmission electron microscopy data (PV-TEM). Monochromatic-cathodoluminescence (mono-CL) was also performed to establish the TDDs in the low-TDD films. The TDD of the highest-TDD ($\sim 2 \times 10^{10}\,cm^{-2}$) film was established by PV-TEM. Van der Pauw Hall, Hall bar, and transmission line measurement (TLM) patterns were then fabricated using optical lithography. For the growth optimization series, Al/Au (30/300 nm) ohmic contacts were deposited by e-beam evaporation, and BCl_3/Cl_2 reactive ion etching was used for mesa isolation. For the TDD-200 and TDD-1000 series, Ti/Al/Ni/Au (20/120/30/50 nm) ohmic contacts were deposited by e-beam evaporation and annealed at 820 °C in an N_2 environment for 30 s to facilitate temperature-dependent Hall measurements. Al/Au (30/300 nm) ohmic contacts were also deposited on both TDD series for RT measurements. BCl_3/Cl_2 reactive ion etching was used for mesa isolation. The carrier concentration, electron mobility, and sheet resistance of the lightly Si-doped n^--GaN layers were determined through Hall measurements. Contact and sheet resistances were determined through TLMs. The sheet resistance from Hall measurements was in close agreement with the results from the TLMs for all samples. Leakage through the isolation layer under the typical measurement biases was negligible.

For the n^--GaN active region, the conductance was calculated to be $\sim$1 mS, and the electron mobility was measured to be $\sim$800 cm^2/Vs (+/− 450 cm^2/Vs). The conductance of the n^+-GaN contact layer was calculated to be about 0.1 mS. From an extrapolation of the carrier concentration versus electron mobility, described later on, the electron mobility of the n^+-GaN contact layer was expected to be less than 300 cm^2/Vs. The impact of a layer on electron mobility in multilayer Hall is proportional to the product of the layer's conductivity and electron mobility.[33] Therefore, the electron mobility

[This article is copyrighted as indicated in the article. Reuse of AIP content is subject to the terms at: http://scitation.aip.org/termsconditions. Downloaded to] IP: 140.112.175.226 On: Tue, 09 Sep 2014 15:31:37

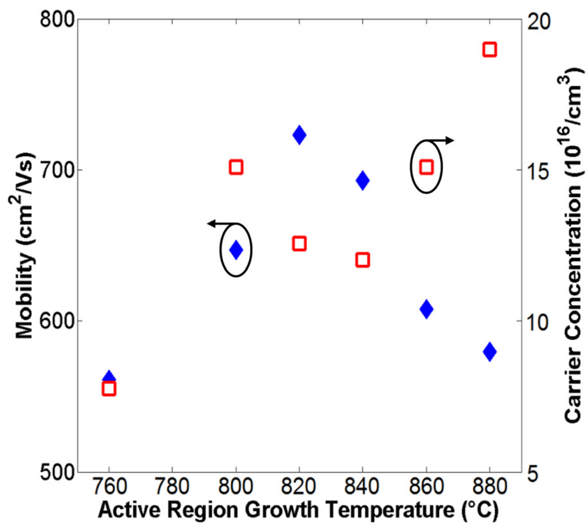

FIG. 2. Average bulk electron mobility (solid blue diamonds) and average carrier concentration (red open squares) as a function of the active region growth temperature in the growth optimization series.

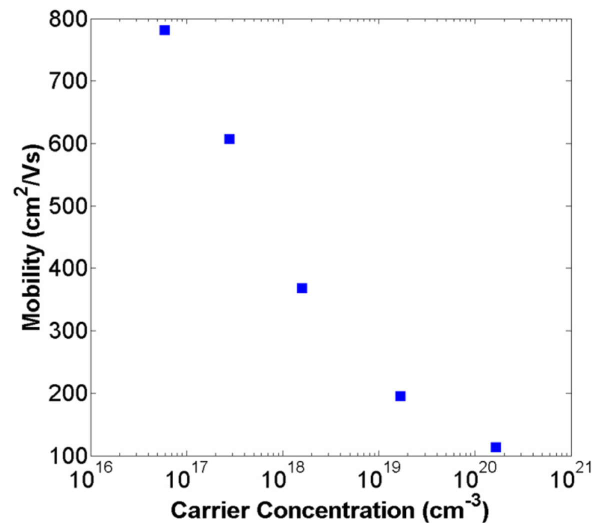

FIG. 4. Effect of carrier concentration on electron mobility for GaN grown with optimized growth conditions. The Si concentration ranged from $\sim 3 \times 10^{16}\,\mathrm{cm}^{-3}$ to $\sim 2 \times 10^{20}\,\mathrm{cm}^{-3}$.

of the n^+-GaN contact layer was negligible in the analysis of the Hall data since its impact on the total measured electron mobility was less than one-twentieth.

III. RESULTS

A. Growth Optimization

Growth temperature and Si-doping concentration were systematically varied to determine their effect on the electron mobility of GaN films. These samples were grown with an NH_3 flow rate of 200 SCCM and a growth rate of ~7.4 nm/min.

First, the dependence of electron mobility and carrier concentration on the active region growth temperature was studied (Fig. 2). As shown in Fig. 2, the electron mobility was found to be highly dependent on growth temperature, with the highest electron mobilities (>700 cm^2/Vs) realized at 820 °C. Thus, 820 °C was determined to be the optimal growth temperature. The AFM images of the growth surface for samples grown at 760 °C, 820 °C, and 880 °C are shown in Fig. 3. At low temperature (760 °C), poor surface diffusion resulted in a rough, pitted surface (Fig. 3(a)). This surface morphology is characteristic of the transition from step-flow growth to layer-by-layer growth in NH_3-MBE.[23] Decomposition of the GaN crystal lattice occurred at a growth temperature of 880 °C, as evidenced by pitting seen in Fig. 3(c). The optimal growth temperature of 820 °C (Fig. 3(b)) was high enough to thermally enhance adatom diffusion, but lower than the onset temperature for GaN decomposition.

Subsequently, the effect of the Si-doping concentration on electron mobility was investigated. The Si concentration was varied from $\sim 3 \times 10^{16}\,\mathrm{cm}^{-3}$ to $\sim 2 \times 10^{20}\,\mathrm{cm}^{-3}$. As expected, the electron mobility decreased with increasing Si-doping concentration (Fig. 4). It should be noted that UID films were not included in this study because ohmic contacts could not be formed. A Si-doping concentration of $\sim 3 \times 10^{16}\,\mathrm{cm}^{-3}$ was found to be the optimal doping concentration for high mobility on templates with TDDs of $\sim 5 \times 10^{8}\,\mathrm{cm}^{-2}$.

B. TDD Series

The effects of TDD variation on electron mobility and carrier concentration were explored after growth

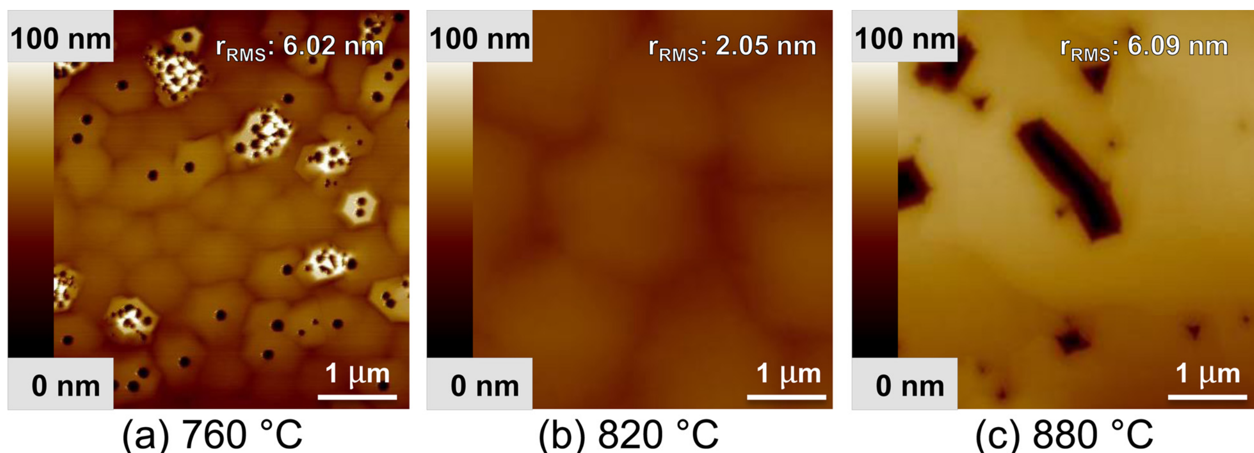

FIG. 3. $5 \times 5\,\mu\mathrm{m}^2$ AFM micrographs of sample surfaces for different active region growth temperatures of (a) 760 °C (b) 820 °C and (c) 880 °C.

[This article is copyrighted as indicated in the article. Reuse of AIP content is subject to the terms at: http://scitation.aip.org/termsconditions. Downloaded to] IP: 140.112.175.226 On: Tue, 09 Sep 2014 15:31:37

TABLE I. Single-die Hall measurements for both TDD series, including the RT electron mobility, the RT carrier concentration, the highest electron mobility, and the temperature at which the highest electron mobility was achieved. FWHMs of the GaN $(20\bar{2}1)\omega$-scans are also included.

TDD-200 Series					
TDD (cm^{-2})	RT mobility (cm^2/Vs)	RT carrier concentration (cm^{-3})	Highest mobility (cm^2/Vs)	Highest mobility temp. (K)	$(20\bar{2}1)$ FWHM (arcsec)
$\sim 3 \times 10^7$	1256	4.48×10^{16}	2948	116	225
$\sim 5 \times 10^8$	961	3.50×10^{16}	2396	115	382
$\sim 5 \times 10^9$	204	4.91×10^{16}	343	154	739
TDD-1000 Series					
TDD (cm^{-2})	RT mobility (cm^2/Vs)	RT carrier concentration (cm^{-3})	Highest mobility (cm^2/Vs)	Highest mobility temp. (K)	$(20\bar{2}1)$ FWHM (arcsec)
$\sim 2 \times 10^6$	1265	3.73×10^{16}	3327	113	90
$\sim 5 \times 10^8$	966	2.09×10^{16}	2637	112	375
$\sim 2 \times 10^{10}$	317	1.33×10^{17}	348	212	1370

optimization. Dislocation-related scattering is known to appreciably reduce bulk electron mobility, even at RT.[18,34,35] Dangling bonds, acting as deep acceptor states, are associated with edge-component TDs.[36] Along the dislocation line, deep acceptor states trap electrons, causing the dislocation to be negatively charged. Although there is no consensus in the literature, the sources of these acceptor states have been identified as gallium vacancies (V_{Ga}) or gallium vacancies complexed with substitutional oxygen impurities ($V_{Ga}-O_N$ or $V_{Ga}-(O_N)_2$).[36,37]

TDD was varied in two growth series: TDD-200 (200 SCCM NH_3 flow rate) and TDD-1000 (1000 SCCM NH_3 flow rate). The TDDs of the GaN layers were varied through growth on GaN templates with differing TDDs. The x-ray rocking curve FWHMs confirming the TDD for each sample in the TDD-200 and TDD-1000 series are shown in Table I. The high-TDD ($\sim 5 \times 10^9\,cm^{-2}$) film in the TDD-200 series was regrown on a GaN-on-6H-SiC template grown by NH_3-MBE. The high-TDD ($\sim 2 \times 10^{10}\,cm^{-2}$) film in the TDD-1000 series was regrown on a GaN-on-6H-SiC template grown by PAMBE.

The TDD-200 series consisted of GaN films with TDDs of $\sim 3 \times 10^7\,cm^{-2}$, $\sim 5 \times 10^8\,cm^{-2}$ and $\sim 5 \times 10^9\,cm^{-2}$. The TDD-1000 series had GaN films with TDDs of $\sim 2 \times 10^6\,cm^{-2}$, $\sim 5 \times 10^8\,cm^{-2}$, and $\sim 2 \times 10^{10}\,cm^{-2}$. All samples were lightly Si doped ([Si] $\sim$3–$5 \times 10^{16}\,cm^{-3}$) except for the high-TDD films, which required Si doping of $\sim$1–$5 \times 10^{17}\,cm^{-2}$ to surpass the high dislocation-related acceptor concentration. The surface morphologies (Fig. 5) showed a positive correlation between root mean square roughness (r_{RMS}) and TDD and a negative correlation between r_{RMS} and NH_3 flow rate. The Hall measurements for both TDD series (Figs. 6, 7, and Table I) show a significant decrease in electron mobility with increasing TDD. This decrease in mobility with increased TDD is due to increased dislocation scattering.

C. Transport and Charge-Balance Model Correlation

In this section, the temperature-dependent electron mobilities and carrier concentrations in the TDD series will be fit to established transport and charge-balance equations. The only fitting parameters that will be used are the acceptor concentration ($[N_A]$), the donor concentration ($[N_D]$), the donor binding energy (E_D), and the occupation of acceptor-like traps along a dislocation (f). All carrier concentrations and electron mobilities will be simultaneously fit to the charge-balance and transport equations self-consistently, using the Levenberg-Marquardt algorithm. For all the equations stated below, parameters not defined in the text are defined in Table II. A correlation between the fitted acceptor concentration and TDD for films grown under identical growth conditions will be found.

First, the charge-balance equation was used to account for compensating acceptors, donors, and free carriers. A one-donor model was assumed for n-GaN; the majority donors, oxygen and silicon, have similar binding energy in GaN.[38] In a non-degenerate n-type semiconductor, the charge-balance equation becomes[39–41]

$$n + N_A^- = N_D^+ = \frac{N_D}{1 + \frac{gn}{N_C}\exp\left[\frac{E_D}{k_B T}\right]}. \quad (1)$$

All of the acceptor states are assumed to be fully ionized as their energy level is far below the Fermi energy level at all studied temperatures. Also, acceptors are assumed to have a single negatively charged state in this analysis. The "apparent" donor binding energy is dependent on donor concentration. It has been suggested that the decrease in donor binding energy with increasing donor concentration is due to the attraction between ionized donors and conduction band electrons.[42] This theory does not consider ionized acceptors which would also affect the donor binding energy.[43] Others have suggested that the decrease in donor binding energy is due to screening of the donor site.[44] Either way, the reduction in donor binding energy is clearly seen in the fitted values for $[N_A]$, $[N_D]$, and E_D in Table III, where smaller donor concentrations correspond to larger apparent donor binding energies.

Table III also lists the sum of the O and Si concentrations measured by secondary ion mass spectroscopy (SIMS) on samples grown under similar conditions with the same Si flux. The measured concentrations of each reported species was at or above the detection limit. The sum of the O and Si

[This article is copyrighted as indicated in the article. Reuse of AIP content is subject to the terms at: http://scitation.aip.org/termsconditions. Downloaded to] IP: 140.112.175.226 On: Tue, 09 Sep 2014 15:31:37

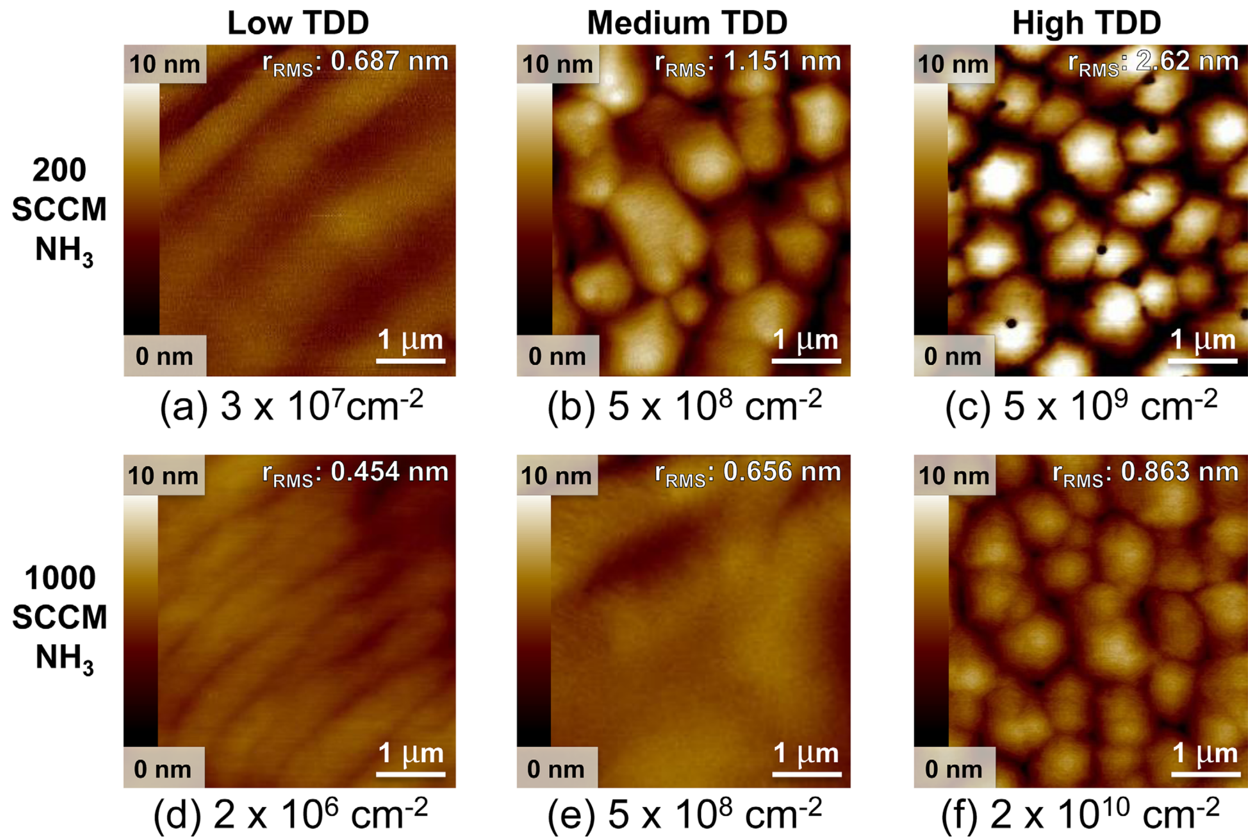

FIG. 5. $5 \times 5\ \mu m^2$ AFM micrographs of sample surfaces for the TDD-200 and TDD-1000 series. The TDDs for the TDD-200 series are (a) $3 \times 10^7\ cm^{-2}$, (b) $5 \times 10^8\ cm^{-2}$, and (c) $5 \times 10^9\ cm^{-2}$. The TDDs for the TDD-1000 series are (d) $2 \times 10^6\ cm^{-2}$, (e) $5 \times 10^8\ cm^{-2}$, and (f) $2 \times 10^{10}\ cm^{-2}$.

concentrations ([O]+[Si]) agreed with the fitted [N_D] in all samples except for the $\sim 5 \times 10^9\ cm^{-2}$ TDD sample in the TDD-200 series. Even for this sample, the fitted donor concentration and [O]+[Si] measured by SIMS are very close. Deep-level optical spectroscopy (DLOS) and Positron Annihilation (PA) are two ways to quantify acceptor concentration. DLOS measures trap concentration as a function of the trap energy. PA measures the concentration of V_{Ga}. This work was in good agreement with acceptor concentrations measured by DLOS and PA, which will be reported separately.[45]

Arrhenius plots of the carrier concentration are shown in Figs. 8 and 9 for both TDD series. Overlaid on these plots are the theoretical fits using the values of [N_A], [N_D], and E_D reported in Table III. Good agreement can be seen between the theoretical fits and the electron concentration curves in Figs. 8 and 9.

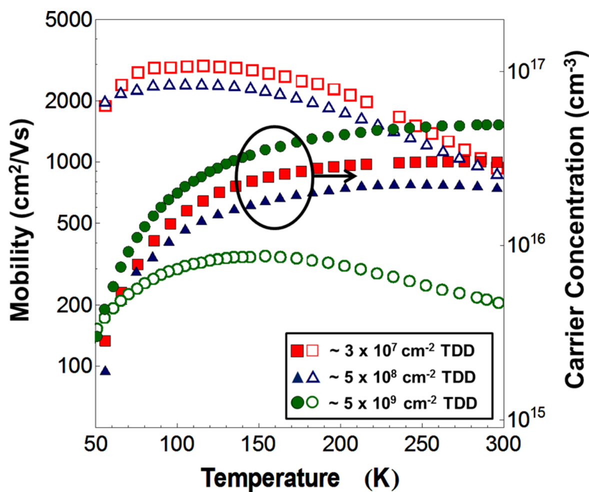

FIG. 6. Temperature-dependent Hall measurements for GaN films grown in the TDD-200 series on high-TDD ($\sim 5 \times 10^9\ cm^{-2}$), medium−TDD ($\sim 5 \times 10^8\ cm^{-2}$), and low-TDD ($\sim 3 \times 10^7\ cm^{-2}$) templates. Electron mobility is shown with open symbols, and carrier concentration is shown with solid symbols.

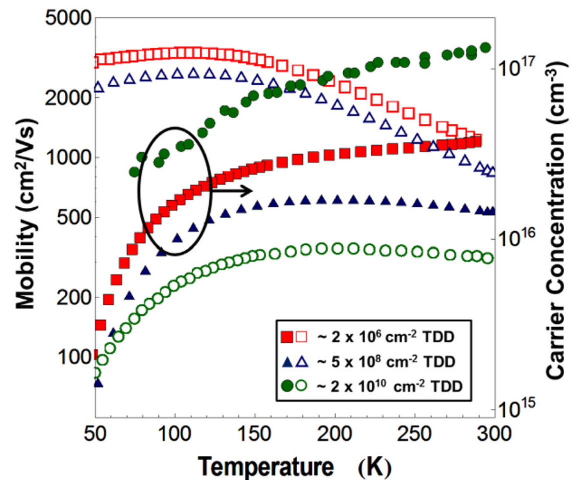

FIG. 7. Temperature-dependent Hall measurements for GaN films grown in the TDD-1000 series on high-TDD ($\sim 2 \times 10^{10}\ cm^{-2}$), medium-TDD ($\sim 5 \times 10^8\ cm^{-2}$), and low-TDD ($\sim 2 \times 10^6\ cm^{-2}$) templates. Electron mobility is shown with open symbols, and carrier concentration is shown with solid symbols.

[This article is copyrighted as indicated in the article. Reuse of AIP content is subject to the terms at: http://scitation.aip.org/termsconditions. Downloaded to] IP: 140.112.175.226 On: Tue, 09 Sep 2014 15:31:37

TABLE II. Constants used in fitting electron mobility data.

Parameter	Symbol	Literature value	References
Degeneracy of the donor state	g	2	53
Effective density of states	N_C	$N_c = 2\left(\frac{2\pi m^* k_B T}{h^2}\right)^{3/2} = 4.98 \times 10^{14} T^{3/2}$ cm^{-3}	62
Apparent donor binding energy	E_D	Calculated for each data set	
Charge state	Z	Defined in text (+/−1)	
Permittivity of free space	ε_0	8.854×10^{-12} F/m	
Static dielectric constant	ε_s	8.9	63
High frequency dielectric constant	ε_∞	5.15	17
Effective mass	m^*	0.22	53, 62, and 64
Electron concentration	n	Experimental	
Boltzmann constant	k_B	8.617×10^{-5} eV/K	
Temperature	T	Experimental	
Charge of electron	q	1.602×10^{-19} C	
Planck constant	h	6.626×10^{-34} Js	
Planck constant	$\hbar$	1.054×10^{-34} Js	
Velocity of light in vacuum	c_{Light}	2.99×10^{8} m/s	
Threading dislocation density	ρ_{TDD}	Experimental	
Average longitudinal elastic constant	c_L	$(8c_{11} + 4c_{13} + 3c_{33} + 8c_{44})/15 = 371$ GPa	46 and 65
Average transversal elastic constant	c_T	$(2c_{11} - 4c_{13} + 2c_{33} + 7c_{44})/15 = 126$ GPa	46 and 65
Elastic constant, c_{11}	c_{11}	390 GPa	65
Elastic constant, c_{13}	c_{13}	106 GPa	65
Elastic constant, c_{33}	c_{33}	398 GPa	65
Elastic constant, c_{44}	c_{44}	105 GPa	65
Deformation potential	D_{ac}	9.2 eV	17 and 66
Piezoelectric constant, element h_x	h_x	$h_{33} - h_{31} - 2h_{15} = 2.02$ C/m^2	46
Piezoelectric constant, element h_{33}	h_{33}	0.73 C/m^2	65, 67, and 68
Piezoelectric constant, element h_{31}	h_{31}	−0.49 C/m^2	65, 67, and 68
Piezoelectric constant, element h_{15}	h_{15}	−0.40 C/m^2	68
E_1 optical phonon energy	E_{pop}	91.1 meV	17
Polar phonon debye temperature(E_1 LO phonon)	T_{LO}	$E_{pop}/k_B = 1057$ K	17
Distance between acceptor-like trap centers along a dislocation	c	5.185Å	68
Occupancy of trap along a dislocation	f	calculated for each data set	
Density of occupied traps along a dislocation line	f/c	calculated for each data set	

Matthiessen's rule was used to approximate the total electron mobility from the individual scattering mechanisms. The scattering mechanisms included: ionized impurity scattering, neutral impurity scattering, dislocation scattering, acoustic deformation potential scattering, piezoelectric scattering, and polar optical phonon scattering. Equations for the scattering rates of these mechanisms were taken from standard references.[41,46,47] Plots of the fitted maximum electron mobility for the individual scattering mechanisms, the fitted total electron mobility, and the measured electron mobility for each sample in the TDD series are shown in Fig. 10.

The Brooks-Herring (BH) technique is the standard approach for calculating ionized impurity scattering for

TABLE III. Donor concentrations, acceptor concentrations, and donor binding energy fitted for the TDD-200 and TDD-1000 series. The sum of [O] and [Si] measured by SIMS are included for comparison to the fitted donor concentrations.

TDD-200 Series				
TDD (cm^{-2})	$[N_A]$ (cm^{-3})	$[N_D]$ (cm^{-3})	E_D (meV)	SIMS [O] + [Si] (cm^{-3})
~3×10^{7}	5.01×10^{15}	3.83×10^{16}	24.12	2–6 $\times 10^{16}$
~5×10^{8}	8.19×10^{15}	3.48×10^{16}	22.09	2–6 $\times 10^{16}$
~5×10^{9}	8.30×10^{16}	1.42×10^{17}	13.29	1.5–1.9 $\times 10^{17}$
TDD-1000 Series				
TDD (cm^{-2})	$[N_A]$ (cm^{-3})	$[N_D]$ (cm^{-3})	E_D (meV)	SIMS [O] + [Si] (cm^{-3})
~2×10^{6}	3.93×10^{15}	4.39×10^{16}	24.10	2–6 $\times 10^{16}$
~5×10^{8}	6.84×10^{15}	2.46×10^{16}	21.18	2–6 $\times 10^{16}$
~2×10^{10}	2.99×10^{17}	4.87×10^{17}	10.46	4.4–4.9 $\times 10^{17}$

[This article is copyrighted as indicated in the article. Reuse of AIP content is subject to the terms at: http://scitation.aip.org/termsconditions. Downloaded to] IP: 140.112.175.226 On: Tue, 09 Sep 2014 15:31:37

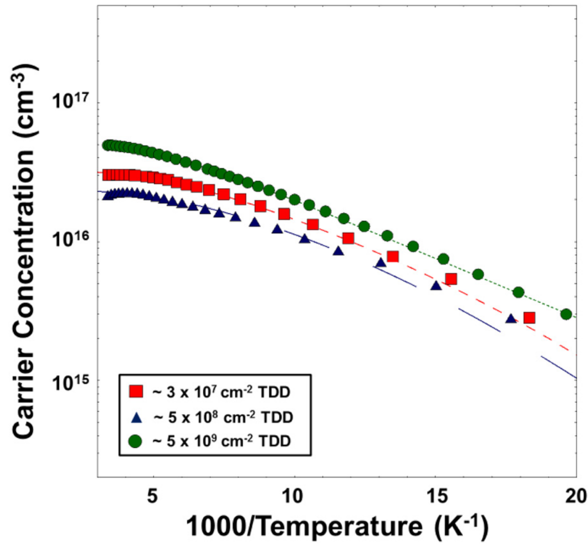

FIG. 8. Fits of the temperature-dependent carrier concentrations for GaN films grown in the TDD-200 series on high-TDD ($\sim 5 \times 10^9\,\mathrm{cm}^{-2}$), medium-TDD ($\sim 5 \times 10^8\,\mathrm{cm}^{-2}$), and low-TDD ($\sim 3 \times 10^7\,\mathrm{cm}^{-2}$) templates.

semiconductors with low ionized impurity concentration. It assumes a screened potential. This assumption requires the screening length for ionized impurities to be much smaller than the average distance between ionized impurities. The screening length was significantly smaller than the average distance between ionized impurities in all samples, proving the validity of the BH approximation for this study. The equation for the ionized-impurity-limited electron mobility using the BH technique is as follows:[41,47]

$$\mu_I = \frac{128\sqrt{2\pi}(\varepsilon_0\varepsilon_s)^2(k_BT)^{3/2}}{N_I Z^2 q^3 \sqrt{m^*}(\ln(1+b) - b/(1+b))}, \tag{2}$$

where b is $24\varepsilon_0\varepsilon_s m^*(k_BT)^2/(\hbar^2 q^2\ n)$. The total ionized impurity concentration is: $N_I = N_D^+ + N_A^-$. The temperature dependence of the ionized donor concentration is given in Eq. (1).

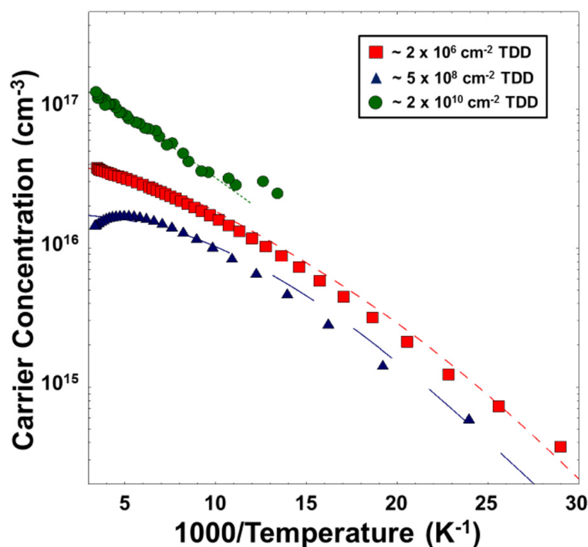

FIG. 9. Fits of the temperature-dependent carrier concentrations for GaN films grown in the TDD-1000 series on high-TDD ($\sim 2 \times 10^{10}\,\mathrm{cm}^{-2}$), medium-TDD ($\sim 5 \times 10^8\,\mathrm{cm}^{-2}$), and low-TDD ($\sim 2 \times 10^6\,\mathrm{cm}^{-2}$) templates.

Neutral impurity scattering was also included. The neutral impurities, N_N, are predominantly un-ionized donors and are accounted for by the following: $N_N = N_{D,Total} - N_D^+$. The ionized donor concentration was calculated from Eq. (1). Erginsoy[48] describes the neutral-impurity-limited electron mobility as

$$\mu_N = \frac{8\pi^3 m^* q^3}{20 N_N \varepsilon_0 \varepsilon_s h^3}. \tag{3}$$

The change in energy during an acoustic phonon scattering event is small compared to the thermal energy of electrons, allowing for the accurate assumption that acoustic phonon scattering is elastic. This model accounts for two types of acoustic phonon scattering: deformation potential and piezoelectric scattering. Acoustic deformation potential scattering is caused by the strain induced to the lattice by acoustic phonons. This strain also creates an electric field in noncentrosymmetric crystals, causing piezoelectric scattering. The acoustic-deformation-potential-limited electron mobility is given as follows:[47]

$$\mu_{DP} = \frac{2\sqrt{2\pi}c_L\hbar^4 q(k_BT)^{-3/2}}{3D_{ac}{}^2(m^{*5/2})}. \tag{4}$$

The piezoelectric-limited electron mobility is given by the following:[41]

$$\mu_{Piez} = \frac{16\sqrt{2\pi}\hbar^2\varepsilon_0\varepsilon_s}{3qP_\perp{}^2(m^{*3/2})\sqrt{k_BT}}, \tag{5}$$

where $P_\perp$ is the perpendicular component of the unitless piezoelectric coefficient for an electric field perpendicular to the c-axis, theoretically given for the wurtzite crystal as[46]

$$P_\perp{}^2 = 4\left(21h_{15}{}^2 + 6h_{15}h_x + h_x{}^2\right)/105\varepsilon_0\varepsilon_s c_T + (21h_{33}{}^2 - 24h_{33}h_x + 8h_x{}^2)/105\varepsilon_0\varepsilon_s c_L. \tag{6}$$

Optical phonon scattering is inelastic, due to the large energy of the optical phonon (~91 meV), and relaxes both the momentum and energy of the electrons. Optical deformation potential scattering does not significantly affect the electron mobility at any temperature considered here and, therefore, was not accounted for in the model. Polar optical phonon scattering becomes the dominant scattering mechanism at high temperatures (>250 K for small impurity-related or TD-related scattering) and must be accounted for despite the inaccuracy of an analytical solution. Iterative methods which account for the energy loss have been developed,[46] but they do not reduce to a closed form solution. Iterative results match well over the temperature range of interest with the expression for electron-limited mobility described by Seeger[41,47]

$$\mu_{POP} = \frac{137q\exp(T_{LO}/T)}{2m^*\sqrt{\frac{m^* c_{Light}{}^2}{2k_BT_{LO}}}\left[\frac{1}{\varepsilon_\infty\varepsilon_o} - \frac{1}{\varepsilon_s\varepsilon_o}\right]\omega_o}. \tag{7}$$

Dislocation scattering in GaN has been thoroughly treated with the Boltzmann transport equation,[35] as well as

[This article is copyrighted as indicated in the article. Reuse of AIP content is subject to the terms at: http://scitation.aip.org/termsconditions. Downloaded to] IP: 140.112.175.226 On: Tue, 09 Sep 2014 15:31:37

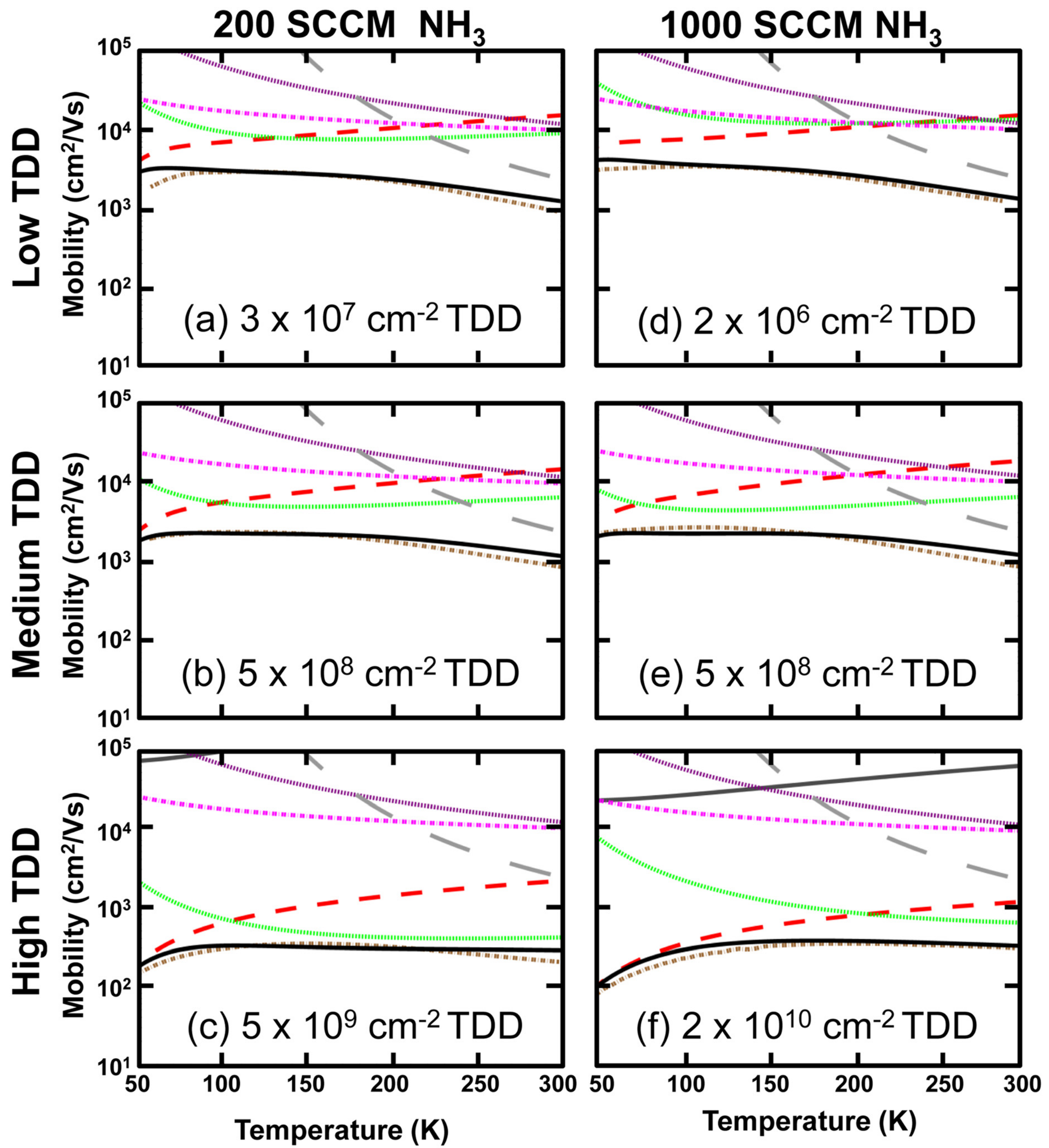

FIG. 10. Electron mobility fitting results for the TDD-200 and TDD-1000 series. The TDDs for the TDD-200 are (a) $3 \times 10^7\,cm^{-2}$, (b) $5 \times 10^8\,cm^{-2}$, and (c) $5 \times 10^9\,cm^{-2}$. The TDDs for the TDD-1000 are (d) $2 \times 10^6\,cm^{-2}$, (e) $5 \times 10^8\,cm^{-2}$, and (f) $2 \times 10^{10}\,cm^{-2}$. The legend for the maximum mobilities limited by individual scattering mechanisms is shown, as well as the legend for the total simulated mobility and the experimentally determined mobility. The reciprocal sum of the maximum mobilities limited by individual scattering mechanisms gives the total simulated mobility. This total mobility agrees well with the experimentally determined mobility. All data were fit using the Levenberg-Marquardt algorithm.

[This article is copyrighted as indicated in the article. Reuse of AIP content is subject to the terms at: http://scitation.aip.org/termsconditions. Downloaded to] IP: 140.112.175.226 On: Tue, 09 Sep 2014 15:31:37

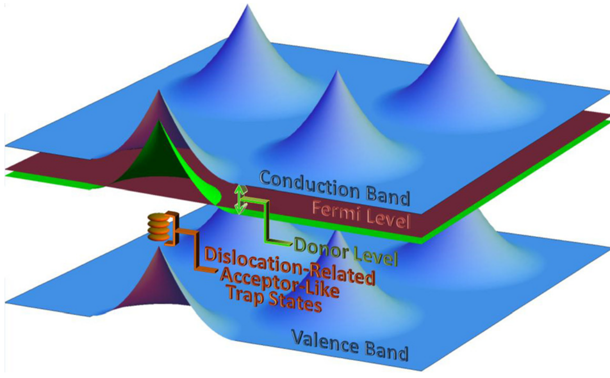

FIG. 11. Illustration of the local band bending around TDs in the n-GaN active region. Dislocations are at the core of the tent-like perturbations. Acceptor-like trap states exist in the dislocation core.

Matthiessen's Rule.[34,49] It is believed that an acceptor-like trap state exists at every *c*-lattice translation along edge-component TDs. When these trap states are ionized, the TD core is negatively charged, creating an electric field surrounding the TD.[35] The core-associated electrostatic potential causes the dislocation-limited electron mobility of[35,50]

$$\mu_{Dis} = \frac{\hbar^3(\varepsilon_0\varepsilon_s)^2 c^2 (1 + 8L_D{}^2 m^* k_B T/\hbar^2)^{3/2}}{\rho_{TDD} q^3 m^{*2} L_D{}^4 f^2}, \quad (8)$$

where L_D is the Debye screening length, described by[50]

$$L_D = \sqrt{\varepsilon_0\varepsilon_s k_B T/(q^2 n')}, \quad (9)$$

where n' is the effective charge screening the negatively charged core of the TD. If the electrostatic potential at the charged dislocation is much larger than k_BT, electrons in the conduction and donor bands surrounding the dislocation will be electrostatically repulsed, depleting the carriers in the vicinity of the dislocation. A positively charged space-charge region of ionized impurities will be left behind and screen the dislocation core. An illustration of the band diagram near a TD is shown in Fig. 11. The energy difference between the donor state and the conduction band does not change with the Fermi level position. Therefore, the donor energy level is lifted far above the Fermi level near the TD, fully depleting all the donor states near the TD. Assuming the electrostatic potential of the TD is less than $E_C - E_A$, all acceptor states will stay fully ionized in the vicinity of the TD. Therefore, the fixed charge surrounding the dislocation will be fully ionized. This space charge then becomes the sum of the total stationary charge in the film ($[N_D]$–$[N_A]$) and is the effective charge screening the dislocation.

Table IV shows the fitted acceptor concentration ($[N_A]$), the occupancy of TD-related acceptor states (f), the distance between occupied acceptor-like trap states along a TD (d_{DIS}), and the concentration of TD-related acceptor states ($[N_{DIS}]$). d_{DIS} and $[N_{DIS}]$ were calculated using the mobility-derived and charge-balance-derived parameters. $[N_{DIS}]$ was calculated using the charge-balance equation, assuming all the acceptor states in the low-TDD samples were unrelated to TDs. It was assumed that the concentration of non-TD-related acceptors was the same for the TDD-200 and TDD-1000 series. Continuing with this assumption, $[N_A]$ of the low-TDD sample was subtracted from $[N_A]$ of each of the higher TDD samples to find $[N_{DIS}]$ ($[N_{DIS}] = [N_A(\text{higher TDD})] - [N_A(\text{lowest TDD})]$). To calculate d_{DIS} using the charge-balance derived parameters, the dislocation density was divided by $[N_{DIS}]$ ($d_{DIS} = \rho_{TDD}/[N_{DIS}]$). Using the mobility-derived parameters, d_{DIS} was found by dividing the assumed acceptor spacing of every *c*-lattice translation (*c*) by the occupancy of dislocation-related acceptor states ($d_{DIS} = c/f$). Then, $[N_{DIS}]$ was found using the mobility-derived parameters by dividing the TDD by d_{DIS} ($[N_{DIS}] = \rho_{TDD}/d_{DIS}$). Good agreement between the charge-balanced-determined and mobility-determined $[N_{DIS}]$ and d_{DIS} is shown in Table IV. A positive correlation between $[N_{DIS}]$ and TDD for films in each NH_3 flow rate series was seen.

In this analysis, the carrier concentration was fit to the charge balance equation, Eq. (1). The mobility was fit using Matthiessen's rule ($\mu_{total}{}^{-1} = \Sigma\mu_i{}^{-1}$), where μ_i are the maximum mobilities limited by individual scattering mechanisms, Eqs. (2), (3), (4), (5), (7), and (8). The fitting parameters used were $[N_D]$, $[N_A]$, E_D, and f. All equations were fit concurrently with commercial fitting software using the

TABLE IV. Fitted acceptor concentration ($[N_A]$), occupancy of dislocation-related trap states along a dislocation (f), calculated dislocation-related trap concentration ($[N_{DIS}]$), and calculated spacing between occupied acceptor traps along a dislocation for the TDD-200 and TDD-1000 series.

TDD-200 Series			Charge-balance determined		Mobility determined	
TDD (cm^{-2})	$[N_A]$ (cm^{-3})	f	$[N_{DIS}]$ (cm^{-3})	Trap spacing[a] (Å)	$[N_{DIS}]$ (cm^{-3})	Trap spacing[a] (Å)
$\sim 3 \times 10^7$	5.01×10^{15}	1.309	Assumed 0	N/A	7.58×10^{14}	3.96
$\sim 5 \times 10^8$	8.19×10^{15}	0.335	3.18×10^{15}	15.74	3.23×10^{15}	15.48
$\sim 5 \times 10^9$	8.30×10^{16}	0.643	7.80×10^{16}	6.41	6.21×10^{16}	8.05
TDD-1000 Series			**Charge-balance determined**		**Mobility determined**	
TDD (cm^{-2})	$[N_A]$ (cm^{-3})	f	$[N_{DIS}]$ (cm^{-3})	Trap spacing[a] (Å)	$[N_{DIS}]$ (cm^{-3})	Trap Spacing[a] (Å)
$\sim 2 \times 10^6$	3.93×10^{15}	4.440	Assumed 0	N/A	1.71×10^{14}	1.17
$\sim 5 \times 10^8$	6.84×10^{15}	0.296	2.91×10^{15}	17.16	2.86×10^{15}	17.49
$\sim 2 \times 10^{10}$	2.99×10^{17}	0.421	2.95×10^{17}	6.78	1.63×10^{17}	12.29

[a]Distance between occupied acceptor traps along a dislocation.

[This article is copyrighted as indicated in the article. Reuse of AIP content is subject to the terms at: http://scitation.aip.org/termsconditions. Downloaded to] IP: 140.112.175.226 On: Tue, 09 Sep 2014 15:31:37

Levenberg-Marquardt algorithm.[51] [N_D] was compared to [O] + [Si] and good agreement was seen. [N_A], f, and ρ_{TDD} was used to calculate [N_{DIS}] and d_{DIS} to understand TD-related acceptor states.

IV. DISCUSSION

Tang *et al.*[22] grew GaN by NH_3-MBE at growth rates of 17–34 nm/min with an NH_3 flow rate of 50 SCCM, which is a higher growth rate and a lower NH_3 flow rate than those used in this study. Since we did not study these specific growth rates or NH_3 flow rates, it is difficult to accurately compare their results to our study. Regardless, Tang *et al.*[22] still achieved a reasonable mobility (560 cm^2/Vs at RT) with growth conditions far outside the range of our study, which highlights the wide range of high-quality GaN growth conditions in NH_3-MBE. The highest-reported mobility (952 cm^2/Vs at 145 K) in the work of Tang *et al.*[22] was measured with a carrier concentration of $1 \times 10^{17}\,cm^{-3}$. Tang *et al.* did not explicitly measure TDD, but HRXRD data and mobility fitting suggested that the lowest achieved TDD was near high $10^8\,cm^{-2}$.[22,52] Our results showed that the ideal Si-doping concentration was near low $10^{16}\,cm^{-3}$ for growths on GaN:Fe-on-sapphire templates with TDDs of $\sim 5 \times 10^8\,cm^{-2}$. Films with lower TDD do not require as high donor concentrations to achieve conduction, which decreases ionized impurity scattering. The work of Tang *et al.* is consistent with the work done here; it is necessary to increase donor concentration as TDD is increased to achieve conduction. Even lower donor concentrations ($\sim 8 \times 10^{15}$–$\sim 2 \times 10^{16}\,cm^{-3}$) were shown to still achieve conduction in HVPE-grown samples with TDDs of $\sim 5 \times 10^5\,cm^{-2}$, further exemplifying the correlation between minimal Si-doping concentration for conduction and TDD.[17,53]

From the work of Zhao *et al.*,[18] high-quality GaN films grown by MOCVD on low-TDD GaN templates had a maximum electron mobility of $\sim$3200 cm^2/Vs at 120 K, which is similar to our findings. Zhao *et al.*[18] also measured a considerable increase in electron mobility with reduced TDD.[18] The highest-reported low-temperature electron mobility of 7386 cm^2/Vs at 48 K was realized by Huang *et al.*[53] on a HVPE-grown sample with a TDD of $\sim 5 \times 10^5\,cm^{-2}$.[54] At low temperature, ionized impurity scattering is by far the strongest scattering mechanism and increases in strength with decreasing temperature. The reason for this is twofold. The Debye length increases as the carriers freeze out, weakening the screening around ionized impurities. Carriers also become less energetic with decreasing temperature, causing them to be more strongly scattered. The GaN films reported here have higher donor and acceptor concentrations than the HVPE-grown GaN sample reported by Huang *et al.* and therefore have lower electron mobility at 48 K than the HVPE-grown GaN sample.[53]

In our analysis, the simulated mobility matched well with our temperature-dependent Hall measurements. Unlike other models that fit mobility and carrier concentration for only one sample or samples grown by different techniques, we fit all sample measurements simultaneously using the same constants. Look *et al.*[17] saw closer agreement between their model and measured mobility, but their mobility simulation varied parameters that are now considered constants. Although we did not use a numerical solution of the Boltzmann transport equation, the underlying assumption made in this analysis, the relaxation time approximation, was valid for all scattering mechanisms except polar optical phonon scattering. The relaxation time approximation is only valid if the scattering mechanism is either isotropic, elastic, or both. For the polar optical phonon scattering mechanism, we used an approximate solution, which is valid for temperatures much less than the polar phonon Debye temperature (1057 K in GaN[17]).[41] Therefore, the approximations made in our simulations generated limited error in our analysis.

For dislocation scattering, there is a lack of agreement in the literature for the effective charge screening the negatively charged core of the TD. An expression for the effective charge was derived by Merten[55] and subsequently reported by Look *et al.*,[35] using a Maclaurin series approximation for the exponential energy terms for electrostatic potential at the dislocation core (V_D) ($\exp(-u) \cong 1-u$ where u is $q(E_C - V_D)/k_BT$). This approximation is only valid if $u \ll 1$, which means the electrostatic potential from the charged dislocation must be much less than k_BT. Assuming the dislocation-related traps are deep-level acceptor states, and the local concentration of trap states is significant ($E_C - V_D \gg k_BT$), the previous approximation is invalid. Experimental work supports $E_C - V_D \gg k_BT$, with measured electrostatic potential of 2.5 V for edge TDs from electron holography.[56] Electron holography images films through the interaction between electrons and electric fields, an accurate way to measure electrostatic potential around TDs. Electrostatic potentials in this range are consistent with the assumption that all donor and acceptor states around the TD are ionized. The expression for effective charge reported in this paper ([N_D]–[N_A]) was previously reported by Kamieniecki[57] to be valid under these conditions.

The correlation between unintentional acceptor concentration and TDD is shown in Table IV. The acceptor concentration spread for the TDD-200 series ($\sim 5 \times 10^{15}$ - $\sim 8 \times 10^{16}\,cm^{-3}$) was smaller than that for the TDD-1000 series ($\sim 4 \times 10^{15}$ - $\sim 3 \times 10^{17}\,cm^{-3}$) since there was a larger TDD range in the TDD-1000 series. With similar growth conditions in each series, the increased acceptor concentration can be attributed to TD-related acceptor states. The TD-related acceptor concentration was seen to clearly increase with increasing TDD. The derived acceptor spacing along a dislocation was expected to be constant with TDD, but there was considerable variability between different TDDs. Agreement was seen between the charge-balance-derived and mobility-derived acceptor spacing along a dislocation for individual data sets. Although universal agreement was not seen between data sets, an acceptor-like trap state was estimated to exist at every *c*-lattice spacing along a TD. This disagreement may be due to a slight discrepancy between the TDD measured by TEM or CL and the actual TDD in the films.

[This article is copyrighted as indicated in the article. Reuse of AIP content is subject to the terms at: http://scitation.aip.org/termsconditions. Downloaded to] IP: 140.112.175.226 On: Tue, 09 Sep 2014 15:31:37

Various experimental techniques have been used to study the charge along TDs, with reported values ranging from 0–2 trapped electrons every c-lattice translation based on the electrostatic potential of the TDD. Scanning Kelvin force microscopy uses tapping mode AFM and measures the surface potential.[58,59] It has shown results ranging from no observation of electrostatic potential charge at TDs to an electrostatic potential of 0.1–0.2 V for TDs in n-GaN.[58,59] Scanning capacitance microscopy is a similar technique, measuring a 1.5–2 V shift near TDs and giving a linear charge density of about one trapped electron every 2 c-lattice translation.[60,61] Effects from the surface and low spatial resolution from the large tip radius compared to the small TD cores will substantially impact the measurement, making the charge measured by scanning Kelvin force microscopy and scanning capacitance microscopy somewhat suspect.[58,59]

The most compelling work on charge associated with TDs was shown by electron holography.[56] This technique has reported two electrons every c-lattice translation along edge TDs in n-GaN, which is within the range presented in this work.[56] The one drawback to this technique is that the distortion near the core of the TD causes the local thickness to be unmeasurable which is needed in the calculation of the local electrostatic potential. It must be assumed that the thickness varies uniformly. If there is surface pitting the potential of the TD will be overestimated.[56]

Although techniques like electron holography and scanning Kelvin force microscopy have locally observed the charge associated with a TD, we have studied the charge associated with TDs over a wide range of growth conditions and TDDs.

V. CONCLUSIONS

The parameters for growth of high-quality GaN by NH_3-MBE were investigated by Hall measurements and AFM. The optimal growth temperature was determined to be 820 °C. The optimal Si-doping concentration was determined to be near $10^{16}\,cm^{-2}$. By fitting the electron mobility and carrier concentration temperature-dependent data with known transport and charge-balance equations, the quality of the films was quantitatively studied. The fitted acceptor concentration was found to correlate with TDD over a wide range ($\sim 2\times10^6$ to $\sim 2\times10^{10}\,cm^{-2}$) of TDDs on films grown under identical conditions. We have shown the highest single die electron mobility of 1265 cm^2/Vs at 296 K for films grown on low-TDD FS GaN templates, the highest RT bulk GaN electron mobility to date.

ACKNOWLEDGMENTS

The authors gratefully acknowledge funding support from the Defense Threat Reduction Agency [Award No. HDTRA1-11-1-0023] (Dr. James Reed, program manager) and the Office of Naval Research (Dr. Paul Maki, program manager). This work made use of the central facilities supported by the NSF MRSEC at UCSB. A portion of this work was done in the UCSB Nanofabrication Facility, part of the NSF-funded *National Nanotechnology Infrastructure Network*. The authors would also like to thank Arthur H. Reading for helpful discussions.

[1]D. Denninghoff, J. Lu, M. Laurent, E. Ahmadi, S. Keller, and U. K. Mishra, in *Proceedings of the 2012 70th Annual Device Research Conference, University Park, Texas, USA, 18-20 June 2012*, pp. 151 and 152.
[2]S. W. Kaun, M. H. Wong, U. K. Mishra, and J. S. Speck, Semicond. Sci. Technol. **28**, 074001 (2013).
[3]L. Shen, Y. Pei, L. McCarthy, C. Poblenz, A. Corrion, N. Fichtenbaum, S. Keller, S. P. Denbaars, J. S. Speck, and U. K. Mishra, in *Proceedings of the 2007 IEEE/MTT-S International Microwave Symposium, Honolulu, Hawaii, USA, 3–8 June 2007*, pp. 623–626.
[4]C. Poblenz, P. Waltereit, S. Rajan, S. Heikman, U. K. Mishra, and J. S. Speck, J. Vac. Sci. Technol., B: Microelectron. Nanometer Struct. **22**, 1145 (2004).
[5]M. H. Wong, S. Keller, N. S. Dasgupta, D. J. Denninghoff, S. Kolluri, D. F. Brown, J. Lu, N. A. Fichtenbaum, E. Ahmadi, U. Singisetti, A. Chini, S. Rajan, S. P. DenBaars, J. S. Speck, and U. K. Mishra, Semicond. Sci. Technol. **28**, 074009 (2013).
[6]A. Tyagi, R. M. Farrell, K. M. Kelchner, C. Huang, P. S. Hsu, D. A. Haeger, M. T. Hardy, C. Holder, K. Fujito, D. A. Cohen, H. Ohta, J. S. Speck, S. P. Denbaars, and S. Nakamura, Appl. Phys. Express **3**, 011002 (2010).
[7]R. Sharma, P. M. Pattison, H. Masui, R. M. Farrell, T. J. Baker, B. A. Haskell, F. Wu, S. P. DenBaars, J. S. Speck, and S. Nakamura, Appl. Phys. Lett. **87**, 231110 (2005).
[8]H. Sato, A. Tyagi, H. Zhong, N. Fellows, R. B. Chung, M. Saito, K. Fujito, J. S. Speck, S. P. Denbaars, and S. Nakamura, Phys. Status Solidi (RRL) **1**, 162 (2007).
[9]P. Waltereit, H. Sato, C. Poblenz, D. S. Green, J. S. Brown, M. McLaurin, T. Katona, S. P. DenBaars, J. S. Speck, J. Liang, M. Kato, H. Tamura, S. Omori, and C. Funaoka, Appl. Phys. Lett. **84**, 2748 (2004).
[10]D. A. Haeger, E. C. Young, R. B. Chung, F. Wu, N. A. Pfaff, M. Tsai, K. Fujito, S. P. DenBaars, J. S. Speck, S. Nakamura, and D. Cohen, Appl. Phys. Lett. **100**, 161107 (2012).
[11]T. Nishida, T. Makimoto, H. Saito, and T. Ban, Appl. Phys. Lett. **84**, 1002 (2004).
[12]T. Miyoshi, S. Masui, T. Okada, T. Yanamoto, T. Kozaki, S. Nagahama, and T. Mukai, Appl. Phys. Express **2**, 062201 (2009).
[13]S. Brüninghoff, C. Eichler, S. Tautz, A. Lell, M. Sabathil, S. Lutgen, and U. Strauß, Phys. Status Solidi A **206**, 1149 (2009).
[14]T. Fujii, Y. Gao, R. Sharma, E. L. Hu, S. P. DenBaars, and S. Nakamura, Appl. Phys. Lett. **84**, 855 (2004).
[15]Y. Lin, M. T. Hardy, P. S. Hsu, K. M. Kelchner, C. Huang, D. A. Haeger, R. M. Farrell, K. Fujito, A. Chakraborty, H. Ohta, J. S. Speck, S. P. Denbaars, and S. Nakamura, Appl. Phys. Express **2**, 082102 (2009).
[16]Y. Yoshizumi, M. Adachi, Y. Enya, T. Kyono, S. Tokuyama, T. Sumitomo, K. Akita, T. Ikegami, M. Ueno, K. Katayama, and T. Nakamura, Appl. Phys. Express **2**, 092101 (2009).
[17]D. C. Look and J. R. Sizelove, Appl. Phys. Lett. **79**, 1133 (2001).
[18]D. G. Zhao, H. Yang, J. J. Zhu, D. S. Jiang, Z. S. Liu, S. M. Zhang, Y. T. Wang, and J. W. Liang, Appl. Phys. Lett. **89**, 112106 (2006).
[19]M. P. D'Evelyn, H. C. Hong, D. Park, H. Lu, E. Kaminsky, R. R. Melkote, P. Perlin, M. Lesczynski, S. Porowski, and R. J. Molnar, J. Cryst. Growth **300**, 11 (2007).
[20]G. Koblmüller, F. Wu, T. Mates, J. S. Speck, S. Fernández-Garrido, and E. Calleja, Appl. Phys. Lett. **91**, 221905 (2007).
[21]B. Heying, I. Smorchkova, C. Poblenz, C. Elsass, P. Fini, S. DenBaars, U. Mishra, and J. S. Speck, Appl. Phys. Lett. **77**, 2885 (2000).
[22]H. Tang and J. B. Webb, Appl. Phys. Lett. **74**, 2373 (1999).
[23]A. L. Corrion, F. Wu, and J. S. Speck, J. Appl. Phys. **112**, 054903 (2012).
[24]R. Quay, *Gallium Nitride Electronics* (Springer, Berlin, 2008), pp. 114 and 115.
[25]C. A. Hurni, J. R. Lang, P. G. Burke, and J. S. Speck, Appl. Phys. Lett. **101**, 102106 (2012).
[26]C. Poblenz, A. L. Corrion, F. Recht, C. S. Suh, R. Chu, L. Shen, J. S. Speck, and U. K. Mishra, IEEE Electron Device Lett. **28**, 945 (2007).

[This article is copyrighted as indicated in the article. Reuse of AIP content is subject to the terms at: http://scitation.aip.org/termsconditions. Downloaded to] IP: 140.112.175.226 On: Tue, 09 Sep 2014 15:31:37

[27]C. A. Hurni, O. Bierwagen, J. R. Lang, B. M. Mcskimming, C. S. Gallinat, E. C. Young, D. A. Browne, U. K. Mishra, and J. S. Speck, Appl. Phys. Lett. **97**, 222113 (2010).
[28]S. Chowdhury, R. Yeluri, C. Hurni, U. K. Mishra, and I. Ben-Yaacov, W. O. patent 177699 (27 December 2012).
[29]J. R. Lang and J. S. Speck, J. Cryst. Growth **346**, 50 (2012).
[30]S. W. Kaun, P. G. Burke, M. H. Wong, E. C. H. Kyle, U. K. Mishra, and J. S. Speck, Appl. Phys. Lett. **101**, 262102 (2012).
[31]A. Corrion, Ph.D. thesis, University of California, Santa Barbara, 2008.
[32]S. W. Kaun, M. H. Wong, S. Dasgupta, S. Choi, R. Chung, U. K. Mishra, and J. S. Speck, Appl. Phys. Express **4**, 024101 (2011).
[33]D. K. Schroder, *Semiconductor Material and Device Characterization*, 3rd ed. (Wiley, New York, 2006), p. 474.
[34]N. G. Weimann, L. F. Eastman, D. Doppalapudi, H. M. Ng, and T. D. Moustakas, J. Appl. Phys. **83**, 3656 (1998).
[35]D. Look and J. Sizelove, Phys. Rev. Lett. **82**, 1237 (1999).
[36]J. Elsner, R. Jones, M. I. Heggie, P. K. Sitch, M. Haugk, T. Frauenheim, S. Oberg, and P. R. Briddon, Phys. Rev. B **58**, 12571 (1998).
[37]J. Oila, J. Kivioja, V. Ranki, K. Saarinen, D. C. Look, R. J. Molnar, S. S. Park, S. K. Lee, and J. Y. Han, Appl. Phys. Lett. **82**, 3433 (2003).
[38]W. Gotz, N. M. Johnson, C. Chen, H. Liu, C. Kuo, and W. Imler, Appl. Phys. Lett. **68**, 3144 (1996).
[39]S. Dhar and S. Ghosh, J. Appl. Phys. **86**, 2668 (1999).
[40]R. Schaub, G. Pensl, M. Schulz, and C. Holm, Appl. Phys. A **34**, 215 (1984).
[41]K. Seeger, *Semiconductor Physics: An Introduction* (Springer, Vienna, 2004).
[42]G. L. Pearson and J. Bardeen, Phys. Rev. **75**, 865 (1949).
[43]P. P. Debye and E. M. Conwell, Phys. Rev. **93**, 693 (1954).
[44]L. Pincherle, Proc. Phys. Soc., A **64**, 663 (1951).
[45]F. Tuomisto, Z. Zhang, A. Arehart, and S. A. Ringel (private communication, 2013).
[46]D. L. Rode, *Semiconductors and Semimetals* (Academic Press, New York, 1975), Vol. 10, pp. 1–89.
[47]M. Grundmann, *Graduate Texts in Physics*, 2nd ed. (Springer, New York, 2010).
[48]C. Erginsoy, Phys. Rev. **79**, 1013 (1950).
[49]D. Zanato, S. Gokden, N. Balkan, B. K. Ridley, and W. J. Schaff, Superlattices Microstruct. **34**, 77 (2003).
[50]B. Pödör, Phys. Status Solidi **16**, K167 (1966).
[51]OriginLab, Origin Pro, version 9.1, a package of data analysis and graphing software, 2013, see http://www.originlab.com/.
[52]H. Tang, J. Webb, J. Bardwell, B. Leathem, S. Charbonneau, and S. Raymond, J. Electronic Mater. **29**, 268 (2000).
[53]D. Huang, F. Yun, M. A. Reshchikov, D. Wang, H. Morkoc, D. L. Rode, L. A. Farina, C. Kurdak, K. T. Tsen, S. S. Park, and K. Y. Lee, Solid-State Electron. **45**, 711 (2001).
[54]P. Visconti, K. M. Jones, M. A. Reshchikov, F. Yun, R. Cingolani, H. Morkoc, S. S. Park, and K. Y. Lee, Appl. Phys. Lett. **77**, 3743 (2000).
[55]L. Merten, Z. Naturforsch. **21**, 793 (1966).
[56]D. Cherns and C. Jiao, Phys. Rev. Lett. **87**, 205504 (2001).
[57]E. Kamieniecki, J. Phys. C: Solid State Phys. **9**, 1211 (1976).
[58]J. W. P. Hsu, H. M. Ng, A. M. Sergent, and S. N. G. Chu, Appl. Phys. Lett. **81**, 3579 (2002).
[59]B. S. Simpkins, D. M. Schaadt, E. T. Yu, and R. J. Molnar, J. Appl. Phys. **91**, 9924 (2002).
[60]P. J. Hansen, Y. E. Strausser, A. N. Erickson, E. J. Tarsa, P. Kozodoy, E. G. Brazel, J. P. Ibbetson, U. Mishra, V. Narayanamurti, S. P. Denbaars, and J. S. Speck, Appl. Phys. Lett. **72**, 2247 (1998).
[61]D. M. Schaadt, E. J. Miller, E. T. Yu, and J. M. Redwing, Appl. Phys. Lett. **78**, 88 (2001).
[62]C. Mavroidis, J. J. Harris, M. J. Kappers, C. J. Humphreys, and Z. Bougrioua, J. Appl. Phys. **93**, 9095 (2003).
[63]M. E. Levinshtein, S. L. Rumyantsev, and M. S. Shur, *Properties of Advanced Semiconductor Materials GaN, AlN, InN, BN, SiC, SiGe* (Wiley & Sons, New York, 2001), p. 1.
[64]P. Perlin, E. Litwin-Staszewska, B. Suchanek, W. Knap, J. Camassel, T. Suski, R. Piotrzkowski, I. Grzegory, S. Porowski, E. Kaminska, and J. C. Chervin, Appl. Phys. Lett. **68**, 1114 (1996).
[65]I. Vurgaftman and J. R. Meyer, J. Appl. Phys. **94**, 3675 (2003).
[66]W. Shan, T. Schmidt, X. H. Yang, J. J. Song, and B. Goldenberg, J. Appl. Phys. **79**, 3691 (1996).
[67]F. Bernardini, V. Fiorentini, and D. Vanderbilt, Phys. Rev. B **56**, R10024 (1997).
[68]A. E. Romanov, T. J. Baker, S. Nakamura, and J. S. Speck, J. Appl. Phys. **100**, 023522 (2006).

[This article is copyrighted as indicated in the article. Reuse of AIP content is subject to the terms at: http://scitation.aip.org/termsconditions. Downloaded to] IP: 140.112.175.226 On: Tue, 09 Sep 2014 15:31:37